Icarus 000 (2016) 1–14

Contents lists available at ScienceDirect

Icarus

journal homepage: www.elsevier.com/locate/icarus

Compositional terranes on Mercury: Information from fast neutrons

David J. Lawrence[a,*], Patrick N. Peplowski[a], Andrew W. Beck[a], William C. Feldman[b], Elizabeth A. Frank[c], Timothy J. McCoy[d], Larry R. Nittler[c], Sean C. Solomon[c,e]

[a] The Johns Hopkins University Applied Physics Laboratory, Laurel, MD 20723, USA
[b] Planetary Science Institute, Tucson, AZ 85719, USA
[c] Department of Terrestrial Magnetism, Carnegie Institution of Washington, Washington, DC 20015, USA
[d] Department of Mineral Sciences, Smithsonian Institution, Washington, DC 20560, USA
[e] Lamont-Doherty Earth Observatory, Columbia University, Palisades, NY 10964, USA

ARTICLE INFO

Article history:
Received 24 February 2016
Revised 12 July 2016
Accepted 24 July 2016
Available online xxx

Keywords :
Mercury
surface

ABSTRACT

We report measurements of the flux of fast neutrons at Mercury from 20°S to the north pole. On the basis of neutron transport simulations and remotely sensed elemental compositions, cosmic-ray-induced fast neutrons are shown to provide a measure of average atomic mass, <*A*>, a result consistent with earlier studies of the Moon and Vesta. The dynamic range of fast neutron flux at Mercury is 3%, which is smaller than the fast-neutron dynamic ranges of 30% and 6% at the Moon and Vesta, respectively. Fast-neutron data delineate compositional terranes on Mercury that are complementary to those identified with X-ray, gamma-ray, and slow-neutron data. Fast neutron measurements confirm the presence of a region with high <*A*>, relative to the mean for the planet, that coincides with the previously identified high-Mg region and reveal the existence of at least two additional compositional terranes: a low-<*A*> region within the northern smooth plains and a high-<*A*> region near the equator centered near 90°E longitude. Comparison of the fast-neutron map with elemental composition maps show that variations predicted from the combined element maps are not consistent with the measured variations in fast-neutron flux. This lack of consistency could be due to incomplete coverage for some elements or uncertainties in the interpretations of compositional and neutron data. Currently available data and analyses do not provide sufficient constraints to resolve these differences.

1. Introduction

One of the primary goals of the MErcury Surface, Space ENvironment, GEochemistry, and Ranging (MESSENGER) mission (Solomon et al., 2008) was to measure the surface elemental composition of Mercury. Surface abundances have been measured and constraints have been placed on the average value and spatial variability of the concentration of many elements on Mercury through a combination of remote sensing techniques. Data from MESSENGER's X-Ray Spectrometer (XRS) and Gamma-Ray and Neutron Spectrometer (GRNS) have provided elemental abundances for H, K, Th, U, and C, and the elemental weight-fraction ratios Na/Si, Mg/Si, Al/Si, S/Si, Cl/Si, Ca/Si, Ti/Si, Cr/Si, Mn/Si, and Fe/Si (Nittler et al., 2011; Peplowski et al., 2011, 2012b, 2012a, 2014, 2015a, 2016; Evans et al., 2012, 2015; Starr et al., 2012; Weider et al., 2012, 2014, 2015; Lawrence et al., 2013a). Measurements of the flux of slow neutrons made with the anticoincidence shield of the Gamma-Ray Spectrometer (GRS) portion of the GRNS have also provided spatially resolved measurements of thermal-neutron-absorbing elements (Peplowski et al., 2015b). Collectively, these data have demonstrated that Mercury has an iron-poor crust, its surface is not depleted in volatile elements (e.g., Na, K, Cl, and S), it has clearly defined compositional terranes, and its geochemical diversity is likely dominated by Mg-rich minerals (Stockstill-Cahill et al., 2012).

Despite this large amount of information, the existing elemental abundance datasets have notable limitations. For many of the measurements, spatial coverage is incomplete and resolution is far from uniform. For example, XRS-derived maps of Mg abundances have nearly global coverage, and resolution in the northern hemisphere is sufficient to discern specific geologic features, but XRS-derived maps of Fe abundances have sparse coverage in the northern hemisphere because only large solar flares, which occur sporadically, can activate the Fe X-ray line. GRS-derived K abun-

* Corresponding author.
E-mail address: david.j.lawrence@jhuapl.edu (D.J. Lawrence).

http://dx.doi.org/10.1016/j.icarus.2016.07.018

dances have been measured north of 20°N and delineate regions of differing composition. However, because of statistical limitations, GRS-derived abundances for other elements yield only latitudinal variations (e.g., Na, Cl) or average values for the northern hemisphere (e.g., S, Fe). All of the elemental datasets have statistical and systematic uncertainties, the magnitude of which vary by element and location. Because of these limitations, compositional information independent of these measurements provides useful additional constraints on the bulk composition of Mercury's surface.

Measurements of planetary fast neutrons constitute a valuable constraint on the bulk composition of Mercury's surface. Fast neutrons, defined as having energies from 0.5 to ~10 MeV, are generated by nuclear spallation reactions when galactic cosmic rays (GCRs) hit the surfaces of airless or nearly airless planetary bodies. On the basis of fast-neutron measurements at the Moon (Maurice et al., 2000, 2004) and the Asteroid Vesta (Lawrence et al., 2013b), along with supporting models of fast neutron generation and transport (Gasnault et al., 2000, 2001; Beck et al., 2015), it has been determined that the energy-integrated flux of fast neutrons from a planetary surface is proportional to the average atomic mass (<A>) of surface material. This relationship between fast neutrons and <A> is effective for determining <A> only if the hydrogen concentration is less than a few hundred parts per million (ppm). Moderate amounts of hydrogen variability (i.e., a few hundred ppm hydrogen) can cause detectable variations in fast neutrons (Lawrence et al., 2013b). Except for the permanently shadowed interiors of craters at Mercury's poles that cover a relatively small area of Mercury's surface (Chabot et al., 2014), we assume here that the hydrogen variability across Mercury's surface satisfies this small-variability condition (this assumption is further discussed in Section 6.1).

On the MESSENGER spacecraft, fast neutrons were measured with the Neutron Spectrometer (NS) portion of the GRNS (Goldsten et al., 2007). Although fast neutrons do not yield element-specific data, the derived map of fast neutron flux from Mercury's surface (Section 4) provides full, spatially resolved coverage of Mercury's equatorial region and northern hemisphere. Only Mg/Si and Al/Si maps have comparable coverage. Other datasets have marked gaps in the northern hemisphere (e.g., Fe/Si, Ca/Si, S/Si) or lack coverage south of ~20°N (e.g., K, slow neutrons). Fast-neutron data are complementary to slow-neutron data, as certain key elements can cause relatively large variations to slow neutrons (e.g., Cl, Gd, Sm) but have little effect on <A> because of their relatively small concentrations.

We present a full-coverage map of fast-neutron variability in Mercury's equatorial region and northern hemisphere and discuss what this map implies for our knowledge of elemental composition variations across Mercury. In Section 2, we discuss in more detail the type of information that is provided by planetary fast neutrons. In Section 3, we provide an overview of the data reduction and processing used to convert the data returned from the NS to a map of relative fast-neutron flux. Details of the data reduction are provided in Appendix A. In the final sections of the paper, we present a fast neutron map and compare this map with planetary fast neutron measurements from the Moon and Vesta, as well as with other measurements of Mercury's surface composition. In particular, this map provides new information about Mercury's elemental composition and compositional terranes.

2. Overview of planetary fast neutron measurements

The first measurements of planetary fast neutrons were carried out at the Moon as part of the Lunar Prospector mission (Maurice et al., 2000). From particle transport models, as well as ground-truth comparison with returned samples (Gasnault et al., 2000, 2001), it was established that for lunar materials the

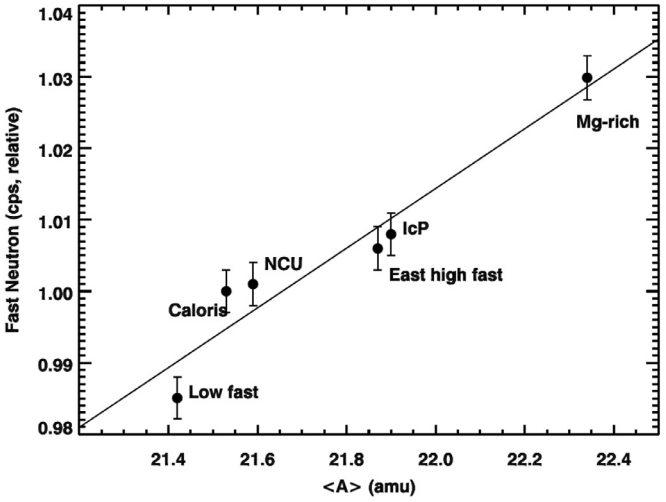

Fig. 1. Calculated fast-neutron count rates, in counts per second (cps) relative to the mean modeled count rates, for varying values of <A>. The different <A> values are determined from XRS and GRS elemental compositions for different regions on Mercury. The locations and specific compositions of these regions are described in Section 6.2. The straight line fit to the data has a slope and offset of 0.042 cps/amu and 0.094 cps, respectively. The error bars represent a statistical uncertainty of 0.3% from the MCNPX Monte Carlo simulation.

measured fast-neutron leakage flux is directly proportional to the soil's average atomic mass, which is defined as:

$$< A >= \sum_i f_i A_i, \quad (1)$$

or equivalently,

$$\frac{1}{< A >} = \sum_i \frac{w_i}{A_i} \quad (2)$$

where, A_i, f_i, and w_i are the atomic mass, mole fraction, and weight fraction for element i, respectively, summed over all elements. For the Moon, the primary control on fast-neutron variability is the variation in iron abundance, and to a lesser extent variability in titanium (Ti) (Maurice et al., 2000). In contrast to the Moon, fast-neutron variability at Mars is driven primarily by variations in hydrogen (H) (Maurice et al., 2011). The reason for this H dependence at Mars is that the concentrations and near-surface depth variations of H are sufficiently large across Mars (greater than a few weight percent water-equivalent H) that energy moderation via neutron scattering dominates the fast-neutron flux variations relative to <A> variations. At Vesta, there are variations in H that are sufficiently large (Prettyman et al., 2012) to cause measurable fast-neutron flux variations. However, these variations were removed from the fast-neutron data from Vesta using an independently measured map of H concentrations (Lawrence et al., 2013b). The remaining fast-neutron variations are consistent with variations in <A> as determined from both orbital data (Peplowski et al., 2013; Prettyman et al., 2013; Yamashita et al., 2013) and expectations from the compositions of howardite, eucrite, and diogenite (HED) meteorites (Beck et al., 2015), which most likely originated from Vesta (McCord et al., 1970; Binzel and Xu, 1993; Russell et al., 2012).

Despite the lack of Mercury samples that could provide a ground-truth comparison for orbital data, compositional measurements from MESSENGER provide clear constraints on the range of elemental abundances present on Mercury. Particle transport simulations of fast-neutron production for Mercury-like soils (Table 1) confirm that the relative fast-neutron flux is proportional to <A> (Fig. 1), as is the case for the Moon and Vesta. As a consequence, information learned from the Moon and Vesta regarding variations

Please cite this article as: D.J. Lawrence et al., Compositional terranes on Mercury: Information from fast neutrons, Icarus (2016), http://dx.doi.org/10.1016/j.icarus.2016.07.018

Table 1
Elemental compositions used for the fast-neutron simulation of Fig. 1 and Mercury's <*A*> element fractions in Fig. 2.

Element	IcP	NCU	High-Mg	Caloris	Low-fast	Eastern high-fast
C	0.0100	0.0100	0.0100	0.0100	0.0100	0.0100
O	0.3845	0.4049	0.3584	0.4147	0.3977	0.3857
Na	0.0275	0.0549	0.0256	0.0296	0.0540	0.0275
Mg	0.1426	0.0842	0.1700	0.0785	0.1346	0.1344
Al	0.0651	0.0709	0.0522	0.0963	0.0716	0.0722
Si	0.2747	0.2892	0.2560	0.2962	0.2840	0.2755
S	0.0214	0.0228	0.0346	0.0181	0.0057	0.0245
Cl	0.0014	0.0043	0.0013	0.0015	0.0023	0.0014
K	0.0004	0.0018	0.0004	0.0004	0.0004	0.0004
Ca	0.0500	0.0451	0.0627	0.0427	0.0281	0.0499
Ti	0.0033	0.0035	0.0031	0.0036	0.0034	0.0033
Cr	0.0014	0.0014	0.0013	0.0015	0.0014	0.0014
Mn	0.0011	0.0012	0.0010	0.0012	0.0011	0.0011
Fe	0.0168	0.0058	0.0236	0.0059	0.0057	0.0127
Th	1.7×10^{-7}	1.4×10^{-7}	1.7×10^{-7}	5.4×10^{-7}	5.4×10^{-7}	5.4×10^{-7}
U	9.0×10^{-8}	9.0×10^{-8}	9.0×10^{-8}	9.0×10^{-8}	9.0×10^{-8}	9.0×10^{-8}
<*A*>	21.90	21.59	22.34	21.53	21.42	21.87

Notes: Compositions are derived from element-to-Si ratios, which are converted to elemental weight fractions by allowing the Si weight fraction to vary so as to reach a weight fraction of 1 for each type. A uniform C concentration is the global-average value reported by Peplowski et al. (2015a) from gamma-ray data. Global average or latitude-dependent concentrations for O, Na, Cl, K, Th, U are taken from gamma-ray data (Evans et al., 2012, 2015; Peplowski et al., 2012b). Limits for Ti, Cr, and Mg are from Nittler et al. (2011). Mg, Al, S, Ca, and Fe concentrations were derived from regional averages of XRS data (Frank et al., 2015; Weider et al., 2015) for different terranes for the regions of interest shown in Fig. 11. IcP denotes intercrater plains; NCU denotes northern composition unit.

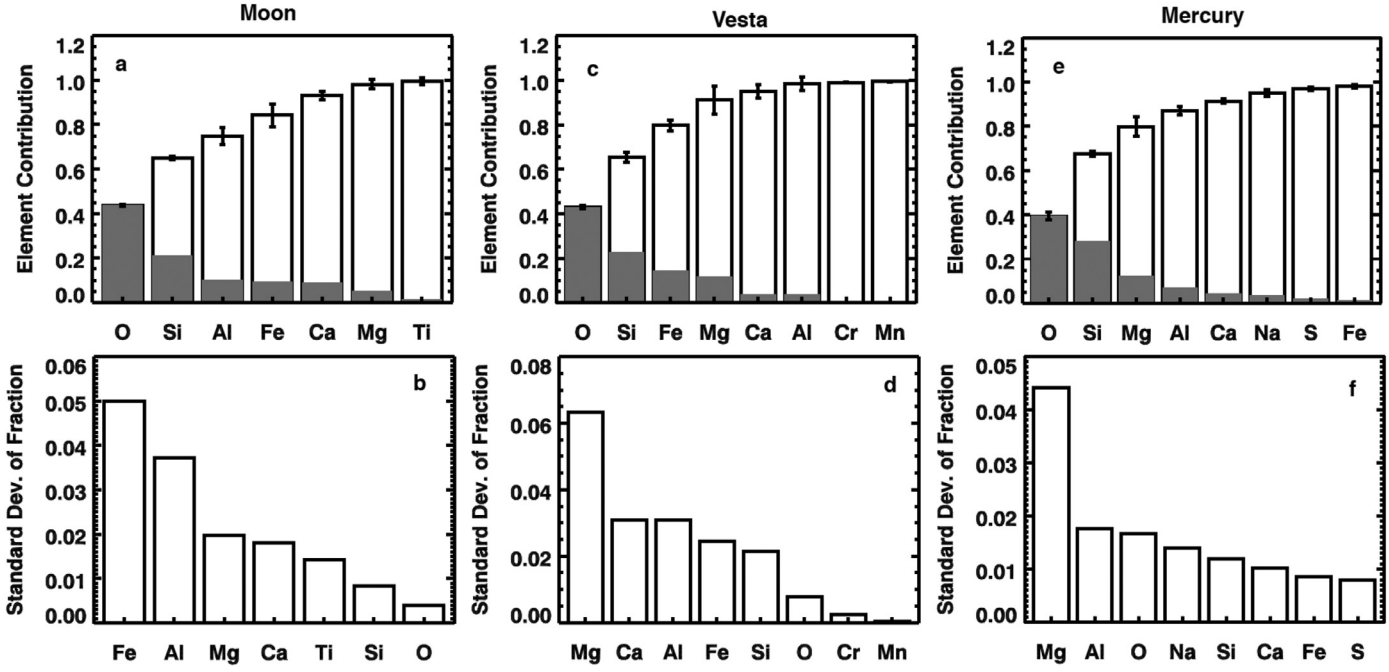

Fig. 2. (Top panels) Cumulative (white bars) and fractional (gray bars) contributions to <*A*> for the global-average surface elemental compositions on (a) the Moon, (c) Vesta, and (e) Mercury. The error bars in (a), (c), and (e) denote the range of elemental variability across each planetary body. (Bottom panels) Elemental variations (taken from the error bars in the top panels) for (b) the Moon, (d) Vesta, and (f) Mercury, sorted by most to least variability. The elemental compositions for the Moon are taken from tables used by Lawrence et al. (2006) and represent different Apollo and Luna sample sites. The elemental compositions for Vesta are taken from Beck et al. (2015) and represent the average compositions for eight different groups and subgroups of HED meteorites. The elemental compositions for Mercury are derived from MESSENGER XRS and GRS data (Table 1).

in fast neutron flux and <*A*> should provide insight for our understanding of Mercury.

The element-specific contributions to <*A*> for average-soil compositions on the Moon, Vesta, and Mercury are shown in Fig. 2. For all three bodies, the largest two contributors to <*A*> are oxygen (O) and silicon (Si) (Fig. 2a, c, e). The reason for this large contribution is that the surfaces of all three bodies are composed of silicate rocks that have large amounts of both O and Si. However, the variations in the concentrations of these elements within the silicate rocks are relatively small, and thus the relative range of variability of $f_i A_i$ is small. We note that the variability of O for Mercury (Fig. 2f) inferred from stoichiometric balancing is larger than that for the Moon and Vesta (Fig. 2b, d).

The variations in <*A*> result from differences in the dominant mineralogies and rock types corresponding to each planetary body. Lunar mineralogy is dominated by variations in four primary

minerals: pyroxene, olivine, plagioclase, and ilmenite (Lucey et al., 2006). The dichotomy between the lunar maria and highlands is the result of large abundances of Fe-rich pyroxenes and olivines and the low abundances of Fe-poor plagioclase in the maria relative to the highlands. Lunar mare regions are thus relatively rich in Fe and Mg and poor in Al and Ca, whereas the reverse is the case in the highlands. Thus, the four most variable elements that contribute to variations in $<A>$ in lunar soils are Fe, Al, Mg, and Ca. Within mare regions, there is a large variability in the abundance of Ti-bearing ilmenite. As a consequence, Ti shows the next largest variability for lunar soils.

There are fewer remote-sensing constraints on Vesta's chemical composition than for the Moon. Consequently, constraints from fast-neutron measurements have proven vital for understanding its surface composition. The three elements with the largest f_iA_i variations are Mg, Ca, and Al. This large variability can be attributed to the fact that Mg has the largest elemental variability in HED compositions (Prettyman et al., 2011) and both Ca and Al are strongly anti-correlated with Mg. The element with the next largest variability is Fe. Combined measurements of fast neutrons and Fe were used to identify a rock type in Vesta's northern hemisphere (Yamato type B diogenites) that is distinct from other lithologies common across Vesta's surface (Beck et al., 2015).

In contrast with the Moon and Vesta, dominant mineralogies for Mercury are unknown, but petrologic modeling (Stockstill-Cahill et al., 2012; Vander Kaaden and McCubbin, 2015) suggests a diversity of permitted minerals that contrasts with the simple system observed on the Moon. Despite these differences, the knowledge gained from the Moon and Vesta can assist in the interpretation of fast-neutron data at Mercury. As with Vesta, the element with the largest f_iA_i variation is Mg, which reflects the large Mg variations across Mercury's surface (Nittler et al., 2011; Weider et al., 2012, 2015) resulting from the predominance of Mg-bearing silicates (enstatite and forsterite) and their variability. Mercury has seven additional elements (Al, O, Na, Si, Ca, Fe, and S) that show comparable variability (within a factor of two). This number is notably greater than for the Moon and Vesta, which have only five and four secondary elements, respectively, with comparable variability. Since coverage of the Mercury composition maps is incomplete for these secondary elements and there are inherent element-specific uncertainties, use of the neutron-derived composition parameters ($<A>$ and neutron absorption) provides important additional constraints.

3. Fast-neutron data reduction

The data reduction procedures used to derive the fast neutron map are similar to those used for previous analyses of MESSENGER neutron data (Lawrence et al., 2010, 2013a; Peplowski et al., 2015b). Compared with studies of orbital neutron data from the Moon, Mars, and Vesta (Maurice et al., 2004, 2011; Prettyman et al., 2012), the reduction and analysis of MESSENGER neutron data are complicated by a number of factors. First, the constantly changing altitude of the MESSENGER spacecraft in its eccentric orbit around Mercury introduces large systematic variations that must be removed from the dataset. Second, the viewing geometry of the MESSENGER NS with respect to Mercury, which is driven by the need always to keep the spacecraft sunshade at a nearly constant orientation relative to the Sun, is highly variable and introduces additional systematic variations that must be removed from the neutron dataset. Finally, in comparison with all other planetary bodies at which neutron measurements have been made, Mercury has the smallest compositional variability, which requires that all corrections be carried out to a high level of precision in order to extract robust compositional information.

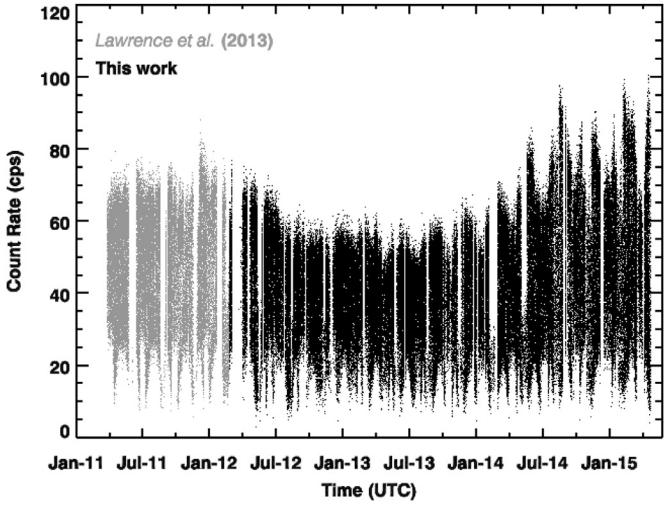

Fig. 3. Measured, uncorrected fast-neutron count rate data from the MESSENGER NS for the full Mercury orbital mission, from 18 March 2011 to 30 April 2015. Gray data points show the data used by Lawrence et al. (2013a); black data points show the additional data used in this study. Data are shown only for altitudes less than 1500 km above Mercury's surface.

To overcome these challenges, we developed a data reduction and analysis framework that used high-fidelity simulations of the measured neutron count rate for a range of neutron energies, including fast neutrons. These simulations account for the planetary neutron creation and transport with the Monte Carlo particle transport code MCNPX (Pelowitz, 2005). The neutron transport from the planet to the spacecraft is calculated by means of the analytic expressions of Feldman et al. (1989). The angle- and energy-dependent response of the MESSENGER NS is simulated with a MCNPX-based geometric model of the full MESSENGER spacecraft. Further details of this framework are provided in Appendix A as well as prior studies (Lawrence et al., 2010, 2013a; Peplowski et al., 2015b).

Although the reduction and analysis of the fast-neutron data given here are similar to the methodology of previous studies, several differences are noteworthy: (1) This study uses a combined 4.5 years of data, whereas (Lawrence et al., 2013a) only used 10 months of data. To illustrate this difference, Fig. 3 shows the raw, uncorrected fast neutron count rate at spacecraft altitudes less than 1500 km, the maximum altitude for which robust measurements of fast neutrons are obtained. This larger dataset provided sufficient statistical precision to obtain the first fast-neutron map for Mercury. (2) Because this dataset covers 4.5 years of time accumulation, the GCR flux variability introduces larger systematic variations in fast-neutron production than were seen in the earlier analysis. A comprehensive analysis of measured GCR variability at MESSENGER was carried out with the GCR-measurement capability of the NS (Rodgers et al., 2015; Lawrence et al., 2016). (3) Following Peplowski et al. (2015b), we implemented a two-dimensional correction for angle- and altitude-dependent NS viewing response. (4) We implemented an improved technique for mapping fast neutrons across Mercury's surface that accounts for the varying spatial resolution.

The NS fast neutron dataset analyzed here consists of 82,962 individual measurements of fast neutron count rates. These measurements have variably sized, frequently overlapping footprints on Mercury's surface. Individual measurements are statistically insignificant, so producing global maps of planetary neutron flux requires spatial re-binning and/or equal-area smoothing to reduce the statistical scatter inherent in the data. Spatial smoothing is often conducted with a spatial footprint that is comparable in size

Please cite this article as: D.J. Lawrence et al., Compositional terranes on Mercury: Information from fast neutrons, Icarus (2016), http://dx.doi.org/10.1016/j.icarus.2016.07.018

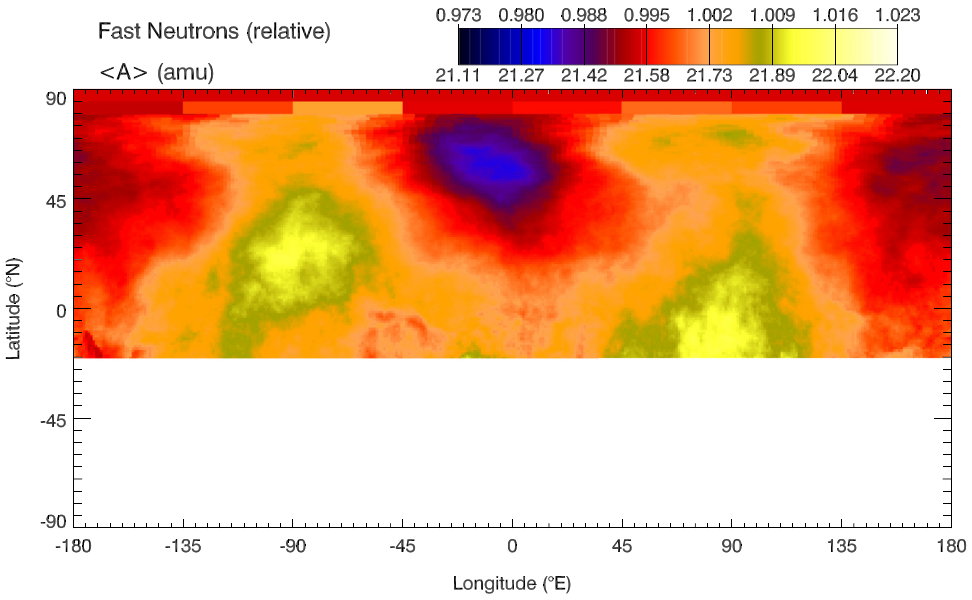

Fig. 4. Map of fast neutron count rates on Mercury relative to the mean value. The scale bar is given in units of relative count rates and $<A>$, where the $<A>$ values are normalized to those inferred at Caloris basin (32°N, 162°E) from mapped XRS and GRS compositional data.

with the actual spatial footprint, which depends on the spacecraft altitude (Lawrence et al., 2003). For all planetary neutron measurements at other Solar System bodies, the size of this footprint was approximately constant across the surface. However, MESSENGER's eccentric orbit around Mercury resulted in a latitude-dependent spatial resolution for the NS dataset. To account for the variable footprint size, the fast neutron map was smoothed with a location-dependent footprint, such that the smoothing footprint at a given location is based on the average spacecraft altitude at that location.

Statistical uncertainties define the southern boundary of the map. Since the MESSENGER orbit always had its periapsis at a high northern latitude, the lowest altitudes are always in the northern hemisphere and the highest altitudes in the southern hemisphere. From statistical studies of simulated count rate maps (see Appendix A) we determined that 20°S is the farthest south that can be mapped with fast neutrons while still obtaining statistically robust results. In the northern hemisphere, the spacecraft's orbital inclination limits sub-spacecraft latitudes to be no farther north than 82.5°N. Nevertheless, because of the large spatial footprint, information is obtained for latitudes farther north than the northernmost sub-spacecraft location. Due in part to data selections on the look direction of the NS, the areal coverage for those northernmost portions of the orbit is limited, which consequently limits statistical precision. As a consequence, for latitudes northward of 70°N, the fast neutron data were not smoothed but were instead re-binned to approximately equal-area pixels ($10° \times 10°$ at the equator, or 420 km by 420 km) to maintain the low statistical uncertainties present at latitudes south of 70°N.

4. Fast-neutron map

The fully reduced map of fast neutron count rates is shown in Fig. 4 and includes a scale for relating fast neutron count rates to $<A>$. This relationship was derived from radiation transport modeling of selected Mercury surface compositions, normalized to the composition of the Caloris basin (Table 1) (i.e., we assume that the $<A>$ value for our Caloris composition is the measured $<A>$ value at the surface inferred from XRS and GRS data). Caloris basin was chosen for this normalization because it is compositionally distinct in multiple types of measurements, it is well mapped by many of the compositional measurements, and a robust value of $<A>$ can be derived from those measurements.

We also derived a map of modeled fast-neutron count rates (Fig. A7a) for a surface with an assumed homogeneous composition. This model captures the systematic variability of the neutron measurements from uncorrected orientation variations for regions away from the north and south edges of the map in the absence of compositional variations. It serves as a test of our data reduction methodology given that (1) modeled neutron count rates well reproduce our measurements (e.g., Lawrence et al., 2013a) and (2) the model was subjected to the same data corrections as the measurements. This model map was created from 15 instances of modeled maps with different pseudo-random Poisson statistics added to understand the average systematic effects of statistical uncertainties. This mean-model map and its associated map of standard deviation values (Fig. A7b) led to the selection of the 20°S southern boundary of the measured data and the need to use the $10° \times 10°$ approximately equal-area pixels for latitudes northward of 70°N (see Appendix A for additional details).

Histograms of the relative count rates for both the measured (Fig. 4) and modeled (Fig. A7a) values are shown in Fig. 5. The measured count rates show a substantially larger dynamic range (3%) than the modeled count rates (0.6%). Because the modeled count rates are corrected to such a small variation, we are confident that the same correction procedures used for the measured data have removed most of the systematic uncertainties and that the remaining variations in the fast neutron measurements reflect compositional variations on Mercury's surface. By the same argument, the variability in the model map (0.6%) provides a good estimate of the systematic variability remaining in the measured map.

The histogram of measured values suggests that there are at least four distinct count-rate populations indicative of populations of materials with distinct $<A>$ values across Mercury's surface. Inspection of the map shows that each of these populations is approximately continuous and corresponds to a compositionally distinct terrane. The lowest-count-rate region corresponds to a location centered on (60°N, 350°E), and the two highest-count-rate regions are at lower latitudes and centered on 90°E and 270°E. Compared with the Moon and Vesta, Mercury has by far the

Please cite this article as: D.J. Lawrence et al., Compositional terranes on Mercury: Information from fast neutrons, Icarus (2016), http://dx.doi.org/10.1016/j.icarus.2016.07.018

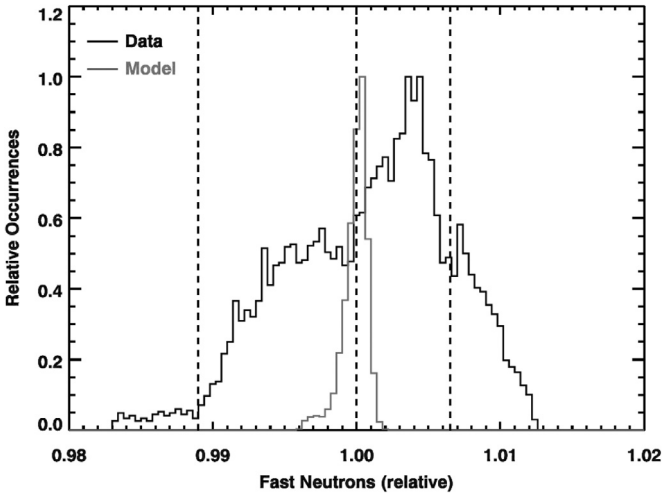

Fig. 5. Histogram of measured (black line) and modeled (gray line) fast neutron count rates relative to the mean value for each map. Vertical dashed lines show the boundaries that define four different compositional groupings on the basis of fast neutron flux.

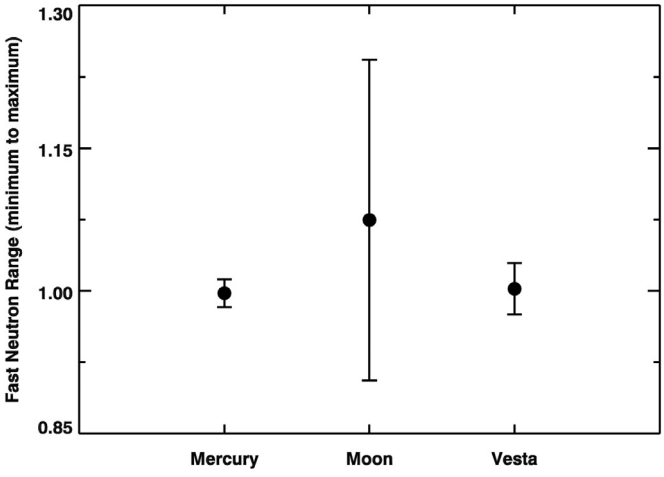

Fig. 6. Relative variations in measured fast neutrons for three airless planetary bodies (Mercury, Moon, and Vesta) at which fast neutrons have been measured. The dynamic range is defined as the maximum and minimum count rates divided by the mean count rates for each respective body.

smallest dynamic range in fast-neutron flux at 3%, versus dynamic ranges at the Moon and Vesta of 30% and 6%, respectively (Fig. 6). The fast-neutron dynamic range within the equatorial regions of Mars is much larger (~75%) but is likely driven mostly by hydrogen variations (Maurice et al., 2011).

5. Comparison of fast-neutron map with morphological and other compositional data

The fast neutron map is compared with a representative set of other Mercury surface characteristics in Fig. 7. Fig. 7a shows contour boundaries of Mercury's major smooth plains units (Denevi et al., 2013) superposed on the fast neutron map. These plains units, which are primarily the product of extensive flood volcanism, are stratigraphically comparable to the lunar maria and by analogy might be expected to correspond to compositionally distinct regions of the surface. Fig. 7a shows a clear association between a lower flux of fast neutrons and the Caloris exterior (CE) plains. The northern portion of these plains shows a slightly lower fast-neutron count rate than the eastern, western, and southern portions. The plains interior to the Caloris basin (CB) and the CE plains are nearly indistinguishable on the basis of fast neutrons, in marked contrast with the clear spectral and compositional differences seen in other datasets. The boundary of the northern smooth plains does not show a clear association with the fast neutron map, consistent with a similar lack of correspondence seen in other compositional measurements.

Fast neutrons are compared with contours of XRS-derived Mg/Si, S/Si, and Ca/Si ratios in Fig. 7b–d. The compositional contours were determined by smoothing the XRS maps through the average spatial response of the fast-neutron measurements. For all three maps, there is a clear correspondence between fast-neutron measurements in the high-Mg region (centered on 20°N, −90°E) and elevated Mg/Si, Ca/Si, and S/Si concentrations. Although less distinct than is the case for the high-Mg region, there is some correspondence between a local high in Mg and local lows in S and Ca concentrations with the lowest fast-neutron count rates (60°N, −10°E). For Ca/Si and S/Si, a lack of good spatial correspondence may be due, in part, to incomplete coverage of the XRS data in this region. Finally, there is a high fast-neutron count-rate region centered near 90°E and the equator that does not have a clear compositional counterpart in the other data, but there may be hint of a compositional variation in the Mg/Si map (Fig. 7b).

To explore the relationship between the fast-neutron data and other element-specific composition measurements, we calculated a "synthetic" fast-neutron map derived from GRS and XRS data. The datasets we used to generate this synthetic map are the Al/Si, Ca/Si, Fe/Si, Mg/Si, and S/Si elemental ratio maps from the XRS (Frank et al., 2015; Weider et al., 2015). In addition, we used latitude-dependent variations of Na/Si (Peplowski et al., 2014) and Cl/Si (Evans et al., 2015) as derived from GRS data. For this exercise, we used Na/Si = 0.1 and 0.19, and we assumed Cl/Si = 0.005 and 0.015 for latitudes south of and north of 50°N, respectively. A global O/Si value of 1.4 was used on the basis of the GRS measurement reported by Evans et al. (2012). Because the spatial footprints are not equal for all datasets or for all locations, we re-binned the available data to approximately equal-area pixels of 420 km by 420 km (or 10° by 10° at the equator). As the spatial coverage is not the same for all maps, a selection was made such that spatial pixels are considered only if there is consistent coverage among all maps. This selection eliminated most of the southern hemisphere because there is no fast-neutron coverage, and it also eliminated large regions in the north-central portion of Mercury that do not have coverage for Ca/Si, S/Si, and Fe/Si. The element-to-Si weight fraction ratios were converted to absolute weight fractions by treating the Si weight fraction, w_{Si}, as a free parameter that was determined by requiring that all the elemental weight fractions to add to 1 on a pixel-by-pixel basis. The derived Si weight fractions ranged from 26 to 29 wt.% and are slightly higher than the values of ~25 wt% and 24.6 wt% used by Nittler et al. (2011) and Evans et al. (2012), respectively. With these weight fractions, calculated values of $\langle A \rangle$ were determined from Eq. (2). The final comparison with the fast-neutron data was made by converting $\langle A \rangle$ to relative fast-neutron count rates with the relation given in Fig. 1.

Histograms of the measured (solid black line) and synthetic fast-neutron count-rate (dashed black line) data are shown in Fig. 8. In both cases, the relative values are normalized to values interior to Caloris basin. The two distributions show a similar shape and width, but they are offset by approximately 1%. We attribute this offset, at least in part, to a mismatch in spatial resolution for the two datasets. Recall that the $\langle A \rangle$-to-fast-neutron calibration was normalized to element compositions and $\langle A \rangle$ values within Caloris basin using, in part, the full-spatial-resolution XRS data, whereas the synthetic $\langle A \rangle$ map was derived from elemental maps with degraded spatial resolution. We applied a final scaling factor of 1.008 to the synthetic fast-neutron count-rate values (solid gray line in Fig. 8) so that the synthetic and measured

Please cite this article as: D.J. Lawrence et al., Compositional terranes on Mercury: Information from fast neutrons, Icarus (2016), http://dx.doi.org/10.1016/j.icarus.2016.07.018

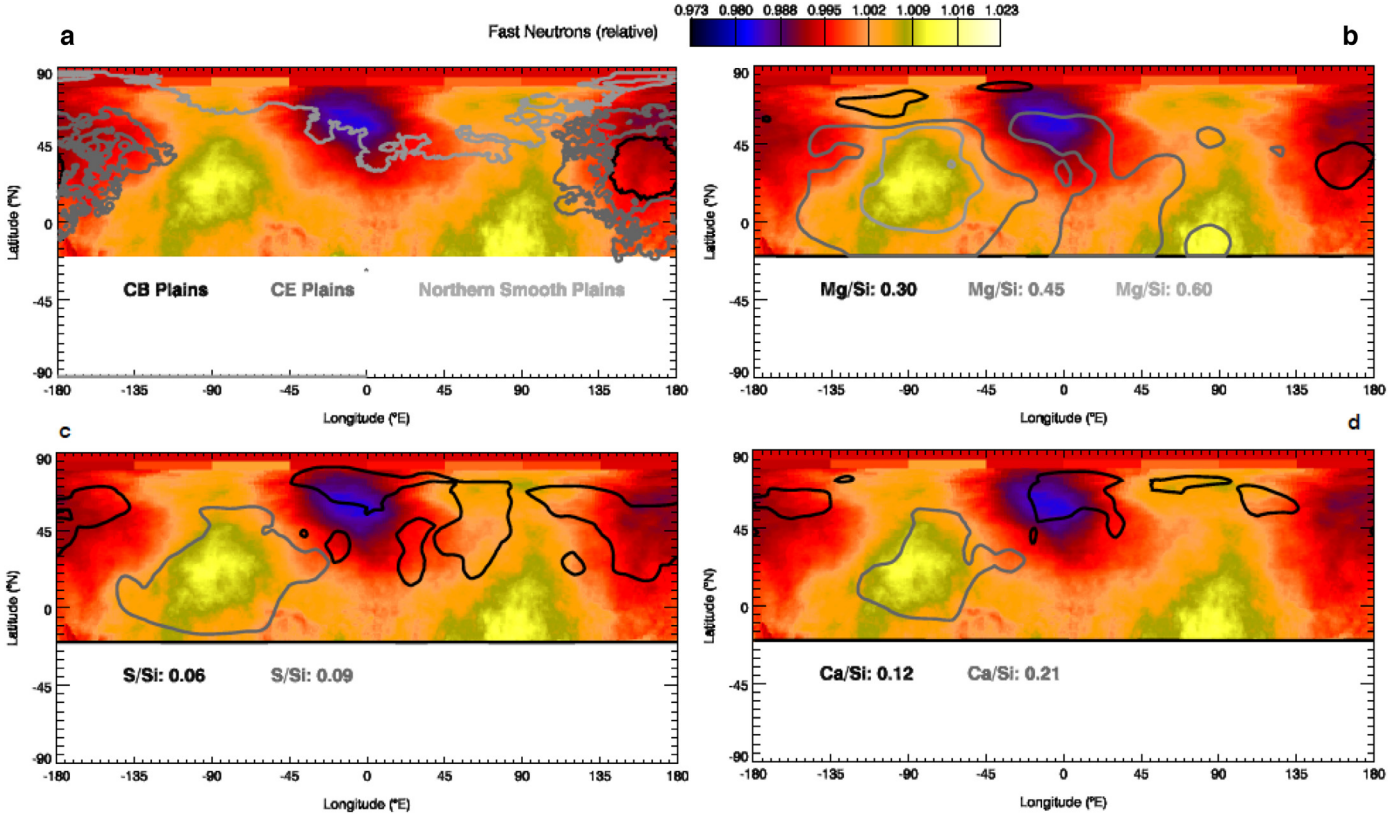

Fig. 7. Measured fast neutrons with overlain contours for (a) smooth plains units (Denevi et al., 2013); (b) Mg/Si ratios; (c) S/Si ratios; and (d) Ca/Si ratios. In (a), the dark contour outlines Caloris basin plains, the dark gray contours outline Caloris exterior plains, and the light gray contours outline the northern smooth plains. In (b), (c), and (d), the color of the contours (black, dark gray, light gray) represent the elemental ratio values as labeled.

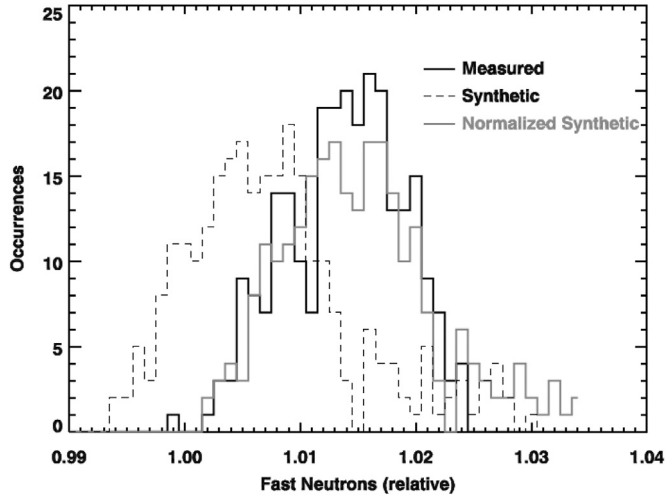

Fig. 8. Histograms of measured and synthetic fast-neutron count rates, relative to the value for the interior of Caloris basin, for regions for which all major elements (except O) and fast neutrons have been measured. Measured fast-neutron count rates are shown with a solid black line, synthetic fast-neutron count rates are shown with a dashed black line, and synthetic fast-neutron count rates after final normalization (described in the text) are shown with a solid gray line.

values largely overlap. This overlap indicates that the dynamic range and spatial distribution of the fast neutrons arise largely from spatial variations in the abundances of individual elements. If it is assumed that this last normalization is appropriate (as appears to be so given the substantial overlap between the measured and synthetic distributions), a clear difference between the two distributions is that the synthetic fast-neutron count-rate distribution shows a population of higher count rates not present in the data.

Maps of the measured and synthetic fast-neutron count rates, the latter with the final normalization of Fig. 8 applied, are shown in Fig. 9. A plot of individual map values of measured versus synthetic count rates is shown in Fig. 10. The synthetic fast-neutron count-rate map shows highs and lows in generally the same locations as the measured fast-neutron count rates, with high rates of fast neutrons in the high-Mg region and low rates of fast neutrons in and around Caloris basin. The measured fast-neutron enhancement near the equator and 90°E has a similar but not identical enhancement in the synthetic map. Despite these broad similarities, there are clear differences. The low-count-rate region in the north-central portion of Mercury is not matched by a similar low in the synthetic fast-neutron count-rate map. However, the coverage of full elemental remote sensing observations in this region is sparse (a few pixels in the southernmost portion of the region), and therefore the calculated values may not be representative of the full region. As shown in Fig. 7d, there are indications that this low fast-neutron count-rate region has relatively low Ca concentrations, which would result in correspondingly lower values of $\langle A \rangle$ and fast-neutron rates. A significant difference between the two maps is in the high-Mg region, where the synthetic fast-neutron rates are notably higher than the measured fast-neutron rates. Inspection of Figs. 9 and 10 shows that the high-Mg region is the source of the high count-rate tail in the histogram of synthetic fast-neutron rates (Fig. 8). If, contrary to the assumption made here, it is assumed that the normalization applied in Fig. 8 is not correct and that the measured fast-neutron count rates match the synthetic values in the high-Mg region, then the synthetic map overestimates the fast-neutron rates in much of the remaining portion of the planet. In either case, the fast-neutron data are not fully consistent with the elemental composition maps.

Please cite this article as: D.J. Lawrence et al., Compositional terranes on Mercury: Information from fast neutrons, Icarus (2016), http://dx.doi.org/10.1016/j.icarus.2016.07.018

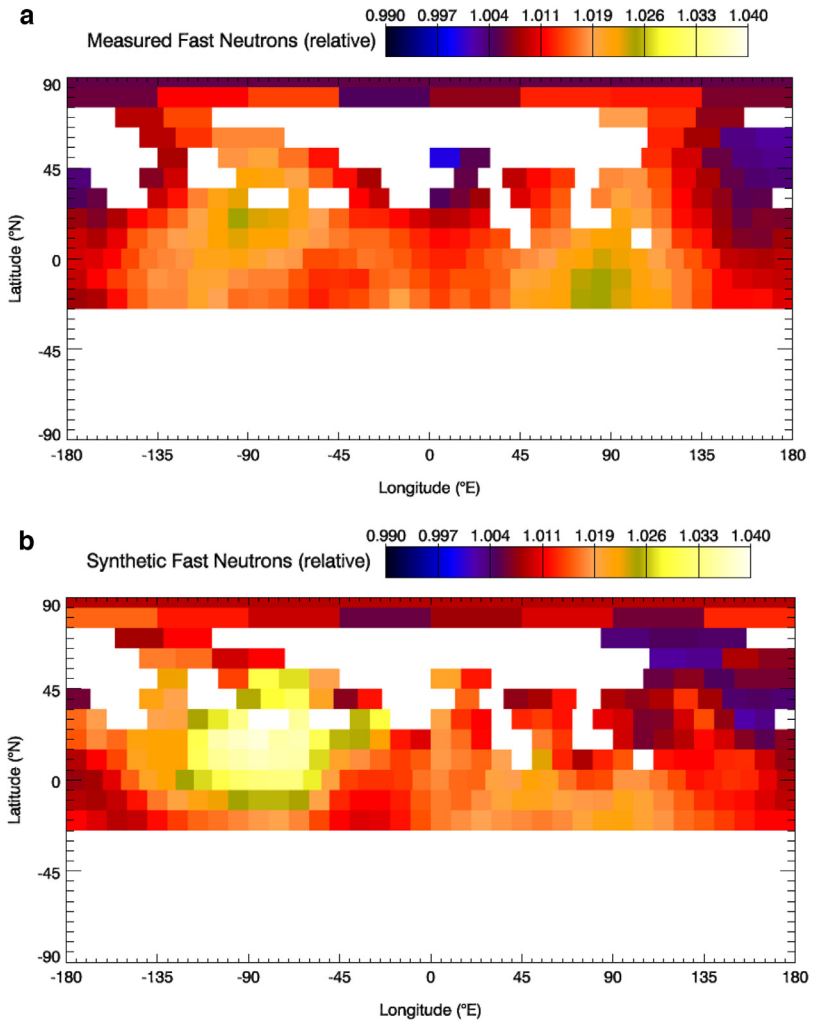

Fig. 9. Maps of (a) measured and (b) synthetic fast-neutron count rates for regions for which all major elements (except O) and fast neutrons have been measured.

6. Discussion

6.1. Synthesis of MESSENGER datasets

We observe notable inconsistencies among the various compositional measurements of Mercury's surface material. These inconsistencies are well illustrated by Figs. 8–10. The most prominent is in the high-Mg region, where the measured fast-neutron count rates are lower by about 1.5% than what is inferred from only the compositional data. If one assumes that the fast-neutron map is correct, one might ascribe the inconsistencies in the high-Mg region (and perhaps other locations) to inaccurate measures of higher-atomic-mass elements, such as Ca or Fe. The lack of constraints for other elements make estimating the possible inaccuracies difficult, as the inputs to <*A*> calculations are underconstrained. As discussed in Section 2 (in connection with Fig. 2f), our current knowledge shows that more elements can affect the variability in <*A*> on Mercury than on either the Moon or Vesta. Whereas Mg and Al appear to be well-constrained, all the other elements in Fig. 2f have at best partial constraints across the full northern hemisphere. In particular, variations in Na and S can cause variations in <*A*>. However, S is only partially mapped, and only latitudinal variations are known for Na. Variations in O and Si can also cause variations in <*A*>. Normally, these elements are not considered as important for studies of elemental variations because their abundances tend to be fairly constant across planetary surfaces. However, even small variations in O can have an impact on <*A*> because its total abundance is so high in silicate materials (generally around 40 to 45 wt%) and it has an atomic mass (16 atomic mass units, or amu) that is substantially below the average

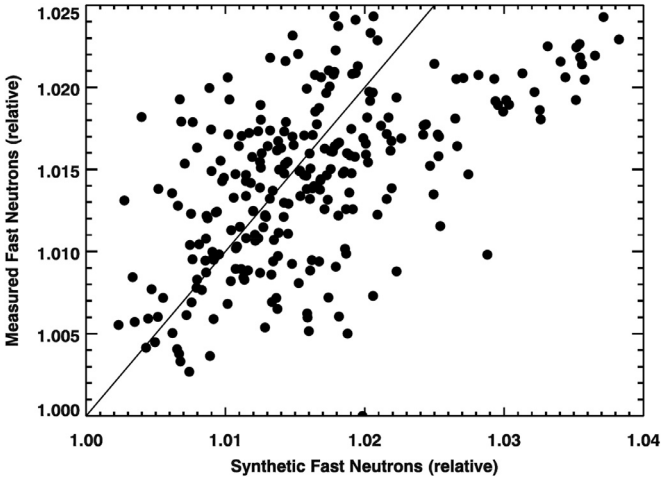

Fig. 10. Synthetic versus measured fast-neutron count rates from the values given in Fig. 9. The solid line has a slope of unity. The correlation coefficient between the two plotted datasets is 0.56.

Please cite this article as: D.J. Lawrence et al., Compositional terranes on Mercury: Information from fast neutrons, Icarus (2016), http://dx.doi.org/10.1016/j.icarus.2016.07.018

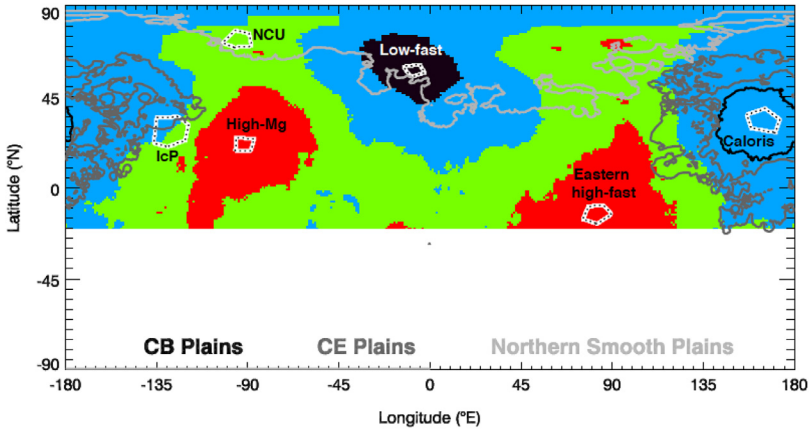

Fig. 11. Mercury's geochemical terrane map derived from the relative fast-neutron count-rate map (Fig. 4). Boundaries of terranes are as follows: < 0.9890 (black area); 0.9890–1.0000 (blue areas); 1.0000–1.0065 (green area); > 1.0065 (red areas). The labeled black and white contours show the regions used for deriving the elemental compositions given in Table 1. Black, dark gray, and light gray contours show the mapped boundaries of the Caloris basin interior plains (CB), Caloris exterior plains (CE), and northern smooth plains, respectively (Denevi et al., 2013).

atomic mass of 21 to 22 amu. Although not normally considered for dry silicate bodies, H can also cause variations in fast neutrons that are unrelated to <*A*>. Given that Mercury is more enriched than expected in volatile elements, one cannot *a priori* rule out spatial variations in H outside the immediate polar regions. As an example, such variability was observed in epithermal neutron data at Vesta (Prettyman et al., 2012). Future studies of epithermal neutron and gamma-ray data should be able to better constrain the non-polar H concentrations on Mercury (Section 7).

Finally, uncertainties and errors in the XRS-derived composition and fast-neutron data should be considered as at least a partial explanation of the inconsistencies. While the fundamental XRS-derived abundances and variations appear robust, second-order non-compositional effects should continue to be investigated. For example, geometric effects and segregation of elements into different minerals may both lead to shifts in the compositions derived by the XRS data analysis procedures (Nittler et al., 2011; Weider et al., 2014). In addition, there may be remaining uncertainties in the unsmoothed XRS data relating to measurements with different mapped footprints that are not fully understood (e.g., Fig. 3a of Weider et al., 2015). Further analysis to probe the accuracy of the derived fast-neutron count-rate map is also warranted. This study has provided a basis for confidence in the compositional variations mapped with fast neutrons. Nevertheless, the fast-neutron map has a very small dynamic range, and although systematic variations from non-compositional factors appear to have been minimized, they might not have been fully removed.

6.2. Geochemical terranes from fast neutrons

The fast-neutron map provides a spatially complete view of the range and location of compositional variability across Mercury's northern hemisphere that complements the element-specific data returned by the GRS and XRS. On the basis of the four compositional groupings identified in Fig. 5, we constructed a fast-neutron map of compositional terranes (Fig. 11). Comparing our results with earlier maps of geochemical terranes, we find that:

- The high-Mg terrane, originally identified with XRS-derived Mg/Si ratios, and seen in maps of Al/Si, Ca/Si, S/Si, and Fe/Si elemental ratios as well as slow neutrons, is also seen in fast neutrons.
- An area in the eastern equatorial region of higher <*A*> than average for Mercury, which has been only hinted in the XRS compositional maps, is clearly delineated with the fast neutrons.
- Fast neutrons delineate a terrane that includes the Caloris exterior (CE) plains and interior Caloris basin (CB) plains. On the basis of other observations, the CB plains were distinctive but the CE plains more closely resemble a composition similar to the average for Mercury. The fast-neutron data show, in contrast, that the lower values of Fe, S, and neutron-absorbing elements within the CB plains are likely compensated by greater abundances of other elements to result in an overall value of <*A*> that is similar to that of the CE plains.
- The fast neutron data delineate a new geochemical terrane mostly within the northern smooth plains that has a lower flux of fast neutrons ("low-fast region"). Weider et al. (2015) suggested the existence of a separate geochemical terrane in this region, but they drew the southern boundary for this terrane to coincide with that of the northern smooth plains. The fast neutron data show that this region lies mostly within the northern smooth plains but its borders do not necessarily coincide with those defined from morphological variations. Additional evidence for the existence of a separate geochemical terrane in this region comes from the concentration of K (Peplowski et al., 2012b), which shows a notable decrease in approximately the same location as the low-fast region.

Given that the low-fast region lies mostly within the northern smooth plains, this observation constitutes evidence for the existence of a compositionally distinct region within those plains, an important constraint for understanding the sources and emplacement history of the volcanic material in this region.

Following Peplowski et al. (2015b), we list the elemental compositions for the terranes identified from fast neutrons in Table 1. These compositions were derived from XRS and GRS maps and were taken from six type regions within the compositional terranes defined by fast neutrons and shown in Fig. 11. These elemental compositions were also those used in the fast-neutron simulations shown in Fig. 1 and the summary of elemental contributions to <*A*> shown in Fig. 2. These elemental compositions provide a new template for future studies that seek to understand the diversity of elemental abundances on Mercury and to carry out modeling studies of mineralogy and source composition.

7. Future work

From the results presented here, what are the next steps for improving our knowledge of the elemental composition of surface material on Mercury? To answer this question, we first reiterate

that whereas <A> does not provide element-specific constraints, the compositional boundaries delineated here provide important information for future studies. Most importantly, these boundaries provide a template through which to derive revised geochemical measurements, particularly from GRS data. MESSENGER GRS data (and any future gamma-ray measurements at Mercury) are limited by counting statistics. In the absence of known compositional boundaries, uncertainties from counting statistics are often reduced by binning the data into large latitude and longitude bins. However, the GRS-derived compositional values for sampling-limited elements such as Na and Cl can be re-investigated for Mercury with the compositional boundaries identified from the fast neutrons. We also note that Peplowski et al. (2012b) reported count-rate maps for O and Si across Mercury's northern hemisphere. Although there was some variability in these maps, this variability was of only marginal statistical significance given the pixel sizes used in the maps. However, it now may be useful to rebin these data on the basis of compositional boundaries defined here to investigate if more significant variations in O and Si abundances can be discerned. Finally, global maps of hydrogen abundance can be derived using both epithermal neutron and gamma-ray data. The challenges for analyzing global epithermal neutron data from the MESSENGER neutron data are similar to those for the fast neutron data reported here. However, the epithermal neutron data have the additional complications of a neutron-velocity Doppler effect that does not affect fast neutrons (Lawrence et al., 2013a). Now that a global fast-neutron study has been completed, work on a global epithermal neutron study can proceed. From gamma-ray data, Peplowski et al. (2015c) demonstrated a new method for indirectly inferring H concentrations from data acquired by the NEAR spacecraft at the Asteroid Eros through analysis of gamma rays arising from both neutron capture and inelastic scattering reactions. In principle, a similar technique could be applied to MESSENGER GRS data to independently derive H concentrations for Mercury's northern hemisphere and compositional terranes delineated by fast neutrons.

Acknowledgments

The MESSENGER project is supported by the NASA Discovery Program under contracts NAS5-97271 to The Johns Hopkins University Applied Physics Laboratory and NASW-00002 to the Carnegie Institution of Washington. Several authors are supported by NASA's MESSENGER Participating Scientist Program. All original data reported in this paper are archived by the NASA Planetary Data System (http://pds-geosciences/wustl.edu/missions/messenger/index.htm).

Appendix A. Fast-neutron data reduction

The data reduction procedures for this study followed an analysis framework similar to that used for previous studies (Lawrence et al., 2010, 2013a; Peplowski et al., 2015b). Fig. A1 shows a flow chart of the different analysis steps, which include parallel paths for the measured and modeled fast-neutron count rates. Modeled fast-neutron count rates were initially derived for spacecraft altitude, h, less than 4000 km and contain data that were collected almost entirely with a 20-s data accumulation period. For the modeled count rates, we added pseudo-random Poisson uncertainties to account for the count-rate uncertainties present in the measured data. Prior to any corrections, selections were made to remove data acquired during solar particle events and energetic electron (EE) events (Lawrence et al., 2015), during which backgrounds are sufficiently high to compromise the neutron measurements. These two selections removed approximately 15% of the total collected data.

Next, selections were made to restrict the viewing geometry in terms of altitude and viewing angles. The altitude was selected to be less than 1500 km, a cutoff that provides measurements with a robust signal-to-background ratio. After a variety of trial-and-error analyses, it was determined that selections for three viewing angles optimized the analysis in terms of reducing systematic variations and providing sufficient statistical precision. These angles and selections were the following: (1) nadir angle (θ_{NA})

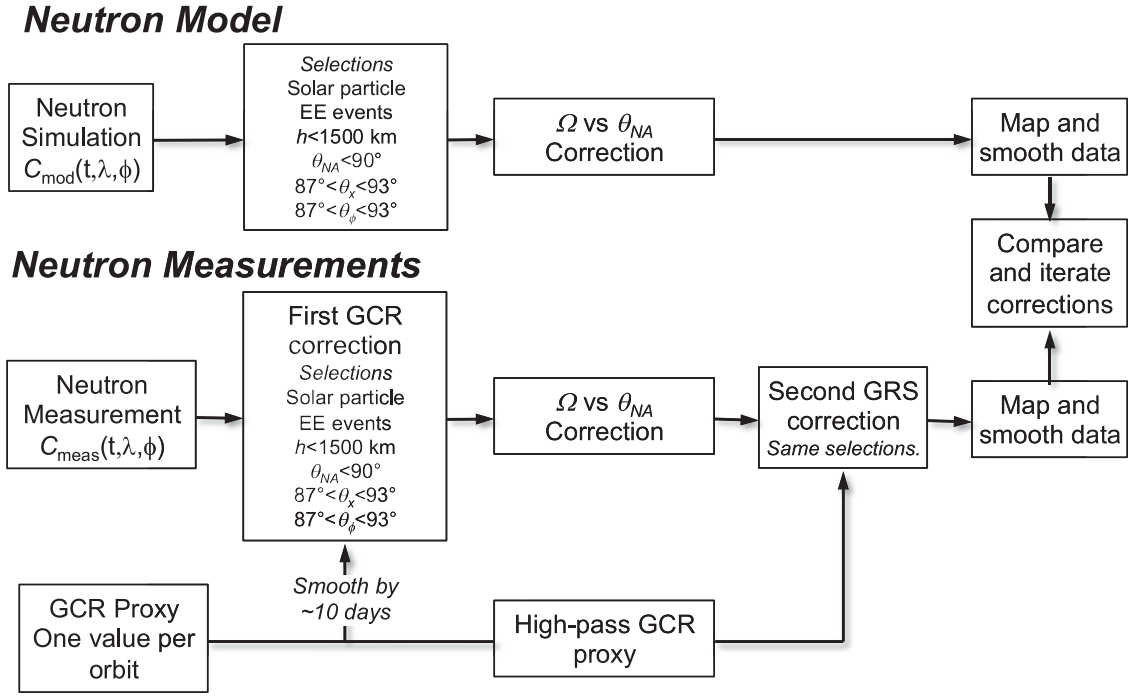

Fig. A1. Flow chart illustrating data reduction steps for fast-neutron analysis. The input values for the analysis are the measured and modeled fast-neutron count rates, which are represented as C_{meas} (t,λ,ϕ) and C_{mod} (t,λ,ϕ), respectively. These count rates depend on time (t) and Mercury-centered latitude (λ) and longitude (ϕ).

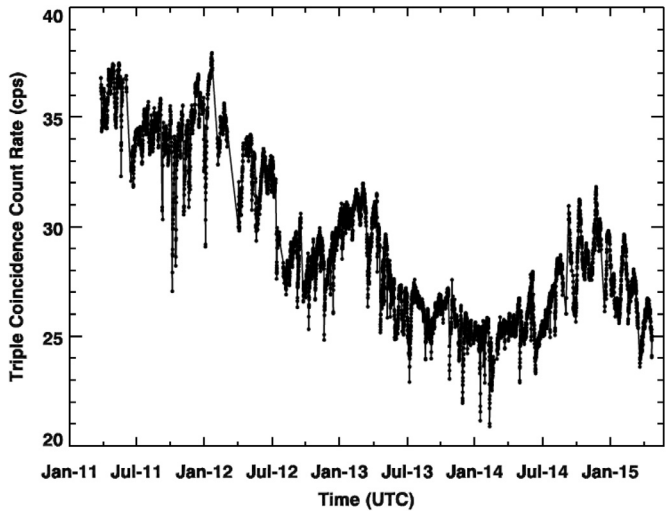

Fig. A2. Time variation in the NS triple-coincidence count rate, which is used as a proxy for GCR variations.

from 0° to 90°, where θ_{NA} is the angle between the spacecraft z-axis and the spacecraft-to-planet-center vector; a description of the MESSENGER spacecraft coordinate system has been given by Leary et al. (2007) and Lawrence et al. (2013a); (2) x-axis angle (θ_x) from 87° to 93°, where θ_x is the angle between the spacecraft x-axis and the spacecraft-to-planet-center vector; and (3) phi angle (θ_ϕ) from 87° to 93°, where θ_ϕ is the azimuthal look direction of the spacecraft in the spacecraft-fixed coordinate system such that $\theta_\phi = 0°$ when the spacecraft x-axis points along the direction of travel. Prior to the viewing geometry selections, there were 1,018,160 20-s measurements at altitudes less than 4000 km. The angular viewing selections reduced this number to 281,478 measurements. The 1500 km altitude cutoff further reduced the number of measurements to 82,962, the number of measurements used to derive the fast-neutron map.

Three corrections were carried out on the data, two of which are corrections for time variations of GCRs. GCR variations (Fig. A2) were determined using the NS triple coincidence count rate, which has been shown to be a good proxy for GCR variations (Rodgers et al., 2015). The average triple-coincidence count rate far from Mercury (altitudes greater than 10,000 km) was calculated for each orbit and interpolated to each near-planet 20-s measurement. Additional corrections to refine the triple-coincidence GCR proxy for spacecraft viewing direction were carried out, and the final GCR proxy was compared with Earth-based GCR measurements for validation. The detailed derivation of the GCR proxy is beyond the scope of this study, but its reduction and validation is described in a separate study (Lawrence et al., 2016).

On the basis of empirical analysis, it was determined that the GCR correction is best carried out in a two-step manner. Corrections for the largest GCR variations were made to the data first. Then, after response corrections were made, a final GCR correction was carried out for smaller variations (see below). For the first of these corrections, the GCR proxy was smoothed in time over intervals of approximately 10 days. This smoothing was done to correct the neutron data for the largest GCR variations. The effects of this correction are seen in Fig. A3, where modeled versus measured data are shown both before (Fig. A3a) and after (Fig. A3b) this GCR correction. Since the modeled values, by definition, have no GCR variations, the non-statistical deviations from the one-to-one line are almost solely due to GCR variations. These variations are notably reduced after the GCR correction.

The next correction accounts for variable instrument response due to different instrument look directions and spacecraft distances to Mercury's surface. Following Peplowski et al. (2015b), we implemented a two-dimensional correction to simultaneously account for variations in response with nadir angle and spacecraft distance. The spacecraft distance was parameterized by the fractional solid angle, Ω, subtended by Mercury in the omnidirectional NS. The measured and modeled two-dimensional response is shown in Fig. A4. That the measured and modeled values are virtually identical provides confidence that the modeled values are properly accounting for the non-GCR count-rate variations. The two-dimensional response correction was accomplished by assigning each fast-neutron measurement a correction factor $R(\Omega,\theta_{NA})$, given in units of counts per second (cps) on the basis of the values in Fig. A4. The fast-neutron count rate was divided by this correction to obtain a relative fast-neutron count rate.

A final correction, mentioned above, was carried out to account for short-term (<10 day) GCR variations. The GCR proxy (Fig. A3) was divided by the smoothed GCR proxy used in the first GCR correction to obtain a high-pass-filtered GCR proxy. This high-pass-filtered GCR proxy correlates with the response-corrected fast-neutron measurements, but not the response-corrected modeled count rates (Fig. A5), which justifies this correction. From binned values of the response-corrected fast-neutron measurements versus high-pass-filtered GCR proxy, a linear correction was derived (dashed line in Fig. A5b) and applied to the measured values.

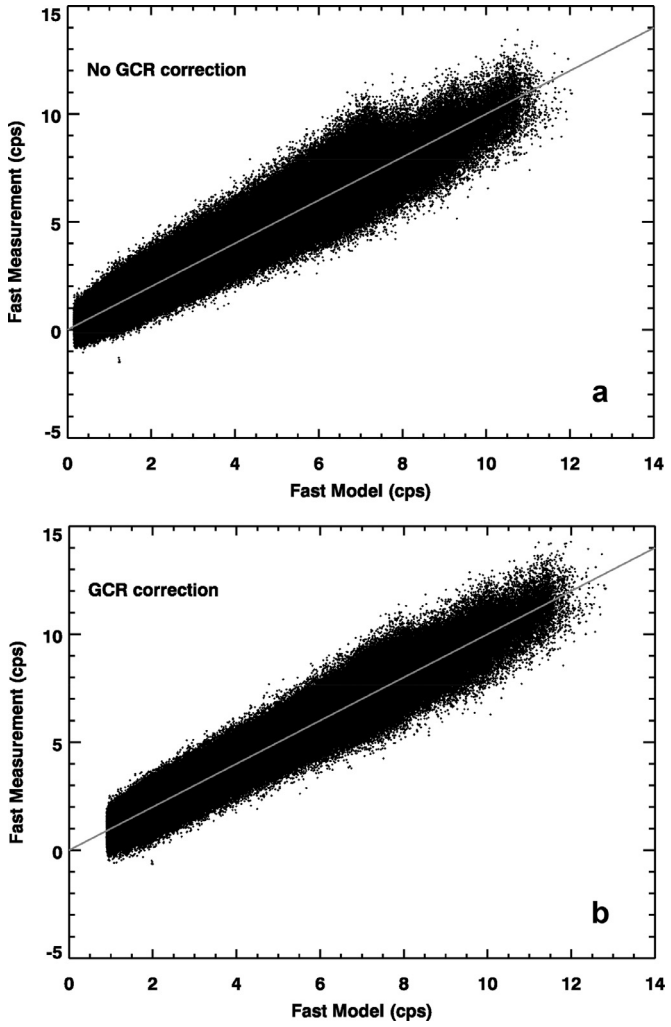

Fig. A3. Fast-neutron measurements versus modeled values (a) before and (b) after the first GCR correction.

Please cite this article as: D.J. Lawrence et al., Compositional terranes on Mercury: Information from fast neutrons, Icarus (2016), http://dx.doi.org/10.1016/j.icarus.2016.07.018

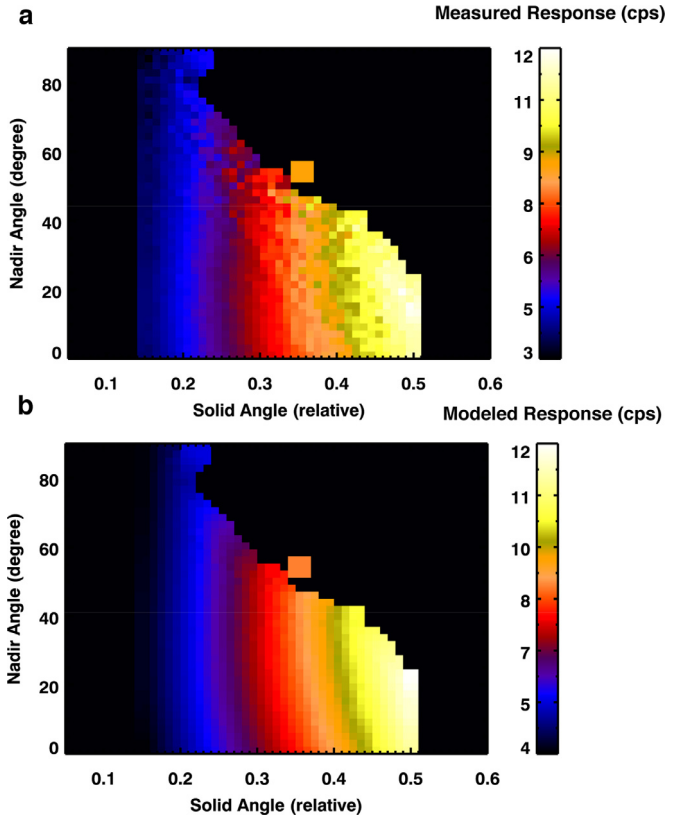

Fig. A4. Solid angle (relative to a value of 1 at the surface of Mercury) versus nadir-angle response for (a) measured and (b) modeled count rates.

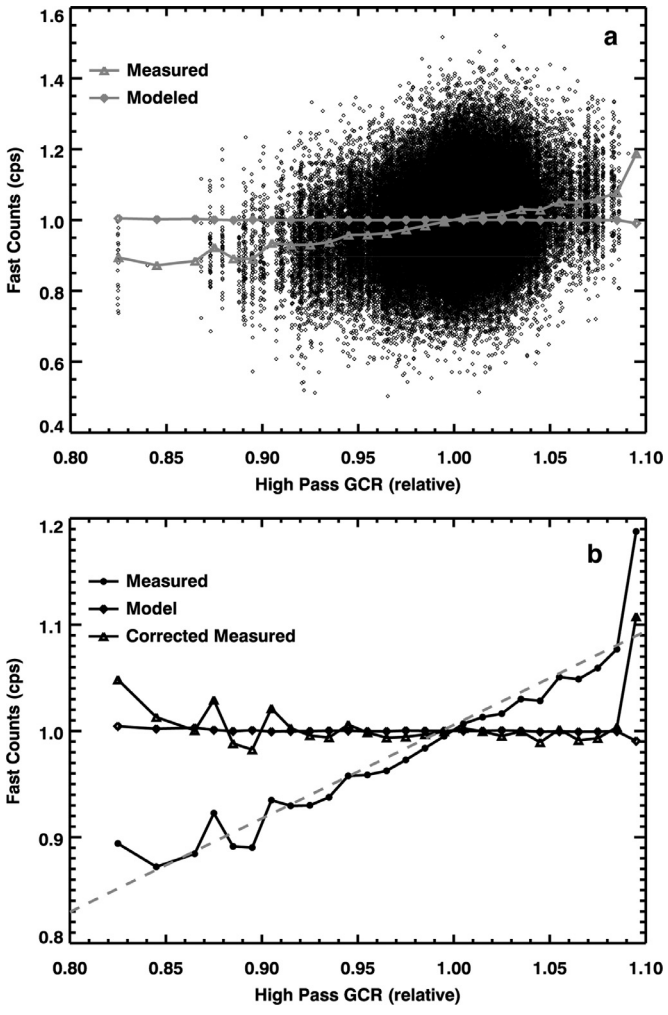

Fig. A5. Measured and modeled fast-neutron counts before and after the second GCR correction. The full set of measured data along with binned values is shown in (a); only binned values are shown in (b).

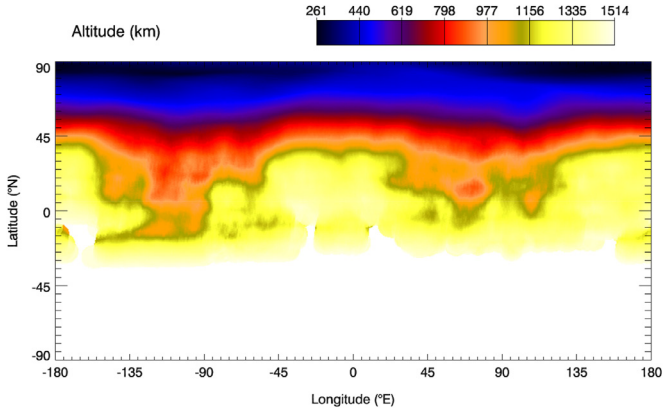

Fig. A6. Map of average altitude (in km) smoothed by a 200-km-radius equal-area smoothing function.

Planetary neutron data are often smoothed to reduce statistical scatter (Lawrence et al., 2003). Normally, neutron data are smoothed using a single spatial footprint because the data are collected from a constant spacecraft altitude. However, for the MESSENGER mission, the altitude was constantly changing, so we implemented a location-dependent, equal-area smoothing algorithm based on the average altitude at each mapping location on the surface. Fig. A6 depicts the approximate location-dependent spatial resolution of the fast-neutron map. Specifically, both the measured and modeled count rates were binned to 0.5°×0.5° pixels and then smoothed such that the smoothing footprint radius was the average altitude at each pixel. The resulting smoothed map was re-binned to 2°×2° equal-area pixels at the equator using the equal-area pixel-size algorithm of Lawrence et al. (2004).

For the modeled count rates, 15 instances of time-series values were derived using independent pseudo-random number deviations to test the sensitivity of the final mapped values to statistical variations. In each instance, we calculated a full simulation of time-series count rates, carried out a full set of data selections and corrections, and mapped and smoothed the modeled count rates. Fig. A7a shows the mean modeled count rate for all 15 instances in a format whereby the relative count rate color scale is the same as for the measured count-rate map in Fig. 4. As reflected in the count rate histograms (Fig. 5), the map is very flat; most deviations are seen near the northern most and southernmost portions of the map, where the spatial coverage after selections is most sparse.

To provide a measure of the systematic uncertainties inherent in the modeled maps resulting from statistical uncertainties, Fig. A7b shows three times the standard deviation of the 15 instances of the model maps. The largest deviations are toward the south and north, which is consistent with the mean model map in Fig. A7a. The standard deviation values are plotted versus latitude in Fig. A8. This figure shows that the three-standard-deviation (3-σ) statistical uncertainties exceed 1% for latitudes poleward of 20°S and 80°N. For larger 10°×10° pixels, the larger number of total counts per pixel reduces the corresponding uncertainties to well below 1%. Since the total variation of the fast neutron count rate on Mercury's surface is approximately 3% (Fig. 5), we adopted a 3-σ limit of $<1\%$ for the statistical uncertainties. It was

Please cite this article as: D.J. Lawrence et al., Compositional terranes on Mercury: Information from fast neutrons, Icarus (2016), http://dx.doi.org/10.1016/j.icarus.2016.07.018

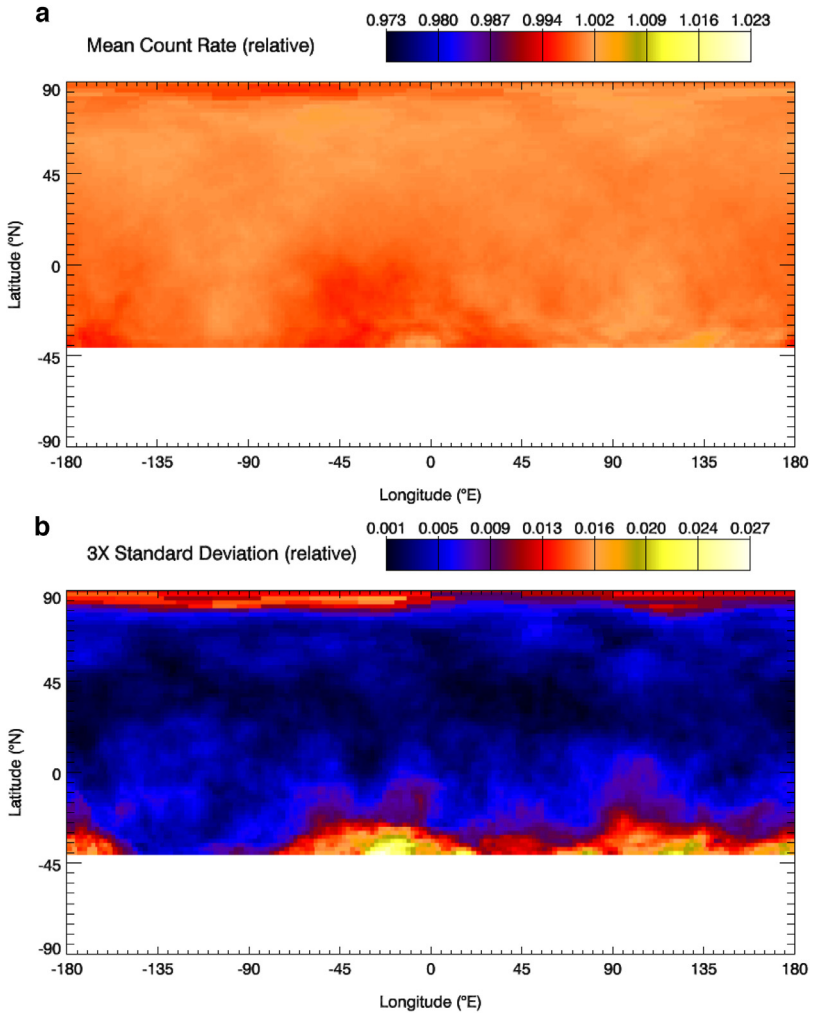

Fig. A7. (a) Map of mean count rates from 15 instances of a model-calculated fast-neutron map. The scale limits of this map are the same as the measured data shown in Fig. 4. (b) Map of three standard deviations of the model-calculated fast-neutron count rates from the 15 instances.

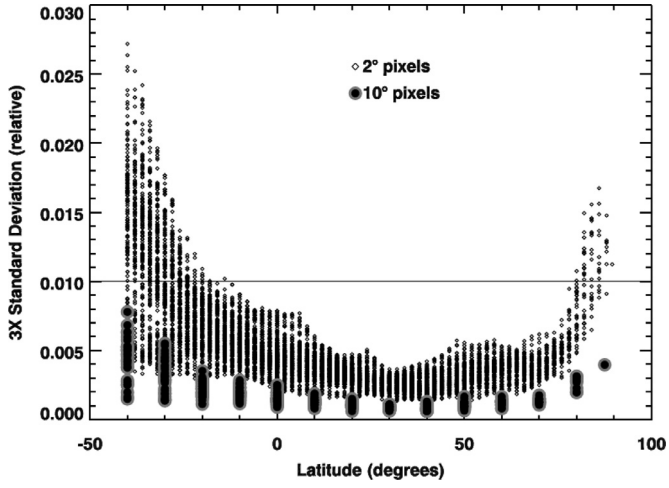

Fig. A8. Three-standard-deviation values versus latitude from the 15 instances of model-calculated fast-neutron maps. Small diamonds show values for approximately equal pixels with a size of $2^{o} \times 2^{o}$ at the equator; large circles show values for approximately equal-area pixels with a size of $10^{o} \times 10^{o}$ at the equator.

this statistical limit that set the 20°S lower latitude limit for the mapped data and drove the decision to use $10^{\circ} \times 10^{\circ}$ equal-area pixels for the northern portion of the fast-neutron map.

References

Beck, A.W., et al., 2015. Using HED meteorites to interpret neutron and gamma-ray data from asteroid 4 Vesta. Meteorit. Planet. Sci. 50, 1311–1337. doi:10.1111/maps.12467.

Binzel, R.P., Xu, S., 1993. Chips off of asteroid 4-Vesta: Evidence for the parent body of basaltic achondrite meteorites. Science 260, 186–191. doi:10.1126/science.260.5105.186.

Chabot, N.L., et al., 2014. Images of surface volatiles in Mercury's polar craters acquired by the MESSENGER spacecraft. Geology 42, 1051–1054. doi:10.1130/G35916.1.

Denevi, B.W., et al., 2013. The distribution and origin of smooth plains on Mercury. J. Geophys. Res. 118, 891–907. doi:10.1002/jgre.20075.

Evans, L.G., et al., 2012. Major-element abundances on the surface of Mercury: Results from the MESSENGER Gamma-Ray Spectrometer. J. Geophys. Res. 117, E00L07. doi:10.1029/2012JE004178.

Evans, L.G., et al., 2015. Chlorine on the surface of Mercury: MESSENGER gamma-ray measurements and implications for the planet's formation and evolution. Icarus 257, 417–427. doi:10.1016/j.icarus.2015.04.039.

Feldman, W.C., et al., 1989. Gravitational effects on planetary neutron flux spectra. J. Geophys. Res. 94, 513–525. doi:10.1029/JB094iB01p00513.

Frank, E.A., et al., 2015. High-resolution measurements of Mercury's surface composition with the MESSENGER X-Ray Spectrometer. In: Lunar Planet. Sci., 46 abstract 1344.

Gasnault, O., et al., 2000. Lunar fast neutron leakage flux calculation and its elemental abundance dependence. J. Geophys. Res. 105, 4263. doi:10.1029/1999JE001124.

Gasnault, O., et al., 2001. Composition from fast neutrons: Application to the Moon. Geophys. Res. Lett. 28, 3797–3800. doi:10.1029/2001GL013072.

Goldsten, J.O., et al., 2007. The MESSENGER Gamma-Ray and Neutron Spectrometer. Space Sci. Rev. 131, 339–391. doi:10.1007/s11214-007-9262-7.

Lawrence, D.J., et al., 2003. Small-area thorium features on the lunar surface. J. Geophys. Res. 108, 5102. doi:10.1029/2003JE002050.
Lawrence, D.J., Maurice, S., Feldman, W.C., 2004. Gamma-ray measurements from Lunar Prospector: Time series data reduction for the Gamma-Ray Spectrometer. J. Geophys. Res. 109, E07S05. doi:10.1029/2003JE002206.
Lawrence, D.J., et al., 2006. Improved modeling of Lunar Prospector Neutron Spectrometer data: Implications for hydrogen deposits at the lunar poles. J. Geophys. Res. 111, E08001. doi:10.1029/2005JE002637.
Lawrence, D.J., et al., 2010. Identification and measurement of neutron-absorbing elements on Mercury's surface. Icarus 209, 195–209. doi:10.1016/j.icarus.2010.04.005.
Lawrence, D.J., et al., 2013a. Evidence for water ice near Mercury's north pole from MESSENGER Neutron Spectrometer measurements. Science 339, 292–296. doi:10.1126/science.1229953.
Lawrence, D.J., et al., 2013b. Constraints on Vesta's elemental composition: Fast neutron measurements by Dawn's gamma ray and neutron detector. Meteorit. Planet. Sci. 48, 2271–2288. doi:10.1111/maps.12187.
Lawrence, D.J., et al., 2015. Comprehensive survey of energetic electron events in Mercury's magnetosphere with data from the MESSENGER Gamma-Ray and Neutron Spectrometer. J. Geophys. Res. Space Phys. 120, 2851–2876. doi:10.1002/2014JA020792.
Lawrence, D.J., et al., 2016. Galactic cosmic ray variations in the inner heliosphere from solar distances less than 0.5 AU: Measurements from the MESSENGER Neutron Spectrometer. J. Geophys. Res. Space Physics 121. doi:10.1002/2016JA022962.
Leary, J.C., et al., 2007. The MESSENGER spacecraft. Space Sci. Rev. 131, 187–217. doi:10.1007/s11214-007-9269-0.
Lucey, P., et al., 2006. Understanding the lunar surface and space-Moon interactions. Rev. Mineral. Geochem. 60, 83–219. doi:10.2138/rmg.2006.60.2.
Maurice, S., et al., 2000. High-energy neutrons from the Moon. J. Geophys. Res. 105, 20365–20375. doi:10.1029/1999JE001151.
Maurice, S., et al., 2004. Reduction of neutron data from Lunar Prospector. J. Geophys. Res. 109, E07S04. doi:10.1029/2003JE002208.
Maurice, S., et al., 2011. Mars Odyssey neutron data: 1. Data processing and models of water-equivalent-hydrogen distribution. J. Geophys. Res. 116, E11008. doi:10.1029/2011JE003810.
McCord, T.B., Johnson, T.V., Adams, J.B., 1970. Asteroid Vesta: Spectral reflectivity and compositional implications. Science 168, 1445–1447. doi:10.1126/science.168.3938.1445.
Nittler, L.R., et al., 2011. The major-element composition of Mercury's surface from MESSENGER X-ray spectrometry. Science 333, 1847–1850. doi:10.1126/science.1211567.
Pelowitz, D.B., 2005. MCNPX User's Manual, version 2.5.0. Los Alamos National Laboratory, Los Alamos, N. Mex., 473 pp.
Peplowski, P.N., et al., 2011. Radioactive elements on Mercury's surface from MESSENGER: Implications for the planet's formation and evolution. Science 333, 1850–1852. doi:10.1126/science.1211576.
Peplowski, P.N., et al., 2012a. Aluminum abundance on the surface of Mercury: Application of a new background-reduction technique for the analysis of gamma-ray spectroscopy data. J. Geophys. Res. 117, E00L10. doi:10.1029/2012JE004181.
Peplowski, P.N., et al., 2012b. Variations in the abundances of potassium and thorium on the surface of Mercury: Results from the MESSENGER Gamma-Ray Spectrometer. J. Geophys. Res. 117, E00L04. doi:10.1029/2012JE004141.
Peplowski, P.N., et al., 2013. Compositional variability on the surface of 4 Vesta revealed through GRaND measurements of high-energy gamma rays. Meteorit. Planet. Sci. 48, 2252–2270. doi:10.1111/maps.12176.
Peplowski, P.N., et al., 2014. Enhanced sodium abundance in Mercury's north polar region revealed by the MESSENGER Gamma-Ray Spectrometer. Icarus 228, 86–95. doi:10.1016/j.icarus.2013.09.007.
Peplowski, P.N., et al., 2015a. Constraints on the abundance of carbon in near-surface materials on Mercury: Results from the MESSENGER Gamma-Ray Spectrometer. Planet. Space Sci. 108, 98–107. doi:10.1016/j.pss.2015.01.008.
Peplowski, P.N., et al., 2015b. Geochemical terranes of Mercury's northern hemisphere as revealed by MESSENGER neutron measurements. Icarus 253, 346–363. doi:10.1016/j.icarus.2015.02.002.
Peplowski, P.N., et al., 2015c. Hydrogen and major element concentrations on 433 Eros: Evidence for an L- or LL-chondrite-like surface composition. Meteorit. Planet. Sci. 50, 353–367. doi:10.1111/maps.12434.
Peplowski, P.N., et al., 2016. Remote sensing evidence for an ancient carbon-bearing crust on Mercury. Nat. Geosci. 9, 273–276. doi:10.1038/ngeo2669.
Prettyman, T.H., et al., 2011. Dawn's Gamma-Ray and Neutron Detector. Space Sci. Rev. 163, 371–459. doi:10.1007/s11214-011-9862-0.
Prettyman, T.H., et al., 2012. Elemental mapping by Dawn reveals exogenic H in Vesta's regolith. Science 338, 242–246. doi:10.1126/science.1225354.
Prettyman, T.H., et al., 2013. Neutron absorption constraints on the composition of 4 Vesta. Meteorit. Planet. Sci. 48, 2211–2236. doi:10.1111/maps.12244.
Rodgers, D.J., et al., 2015. Neutrons and energetic charged particles in the inner heliosphere: Measurements of the MESSENGER Neutron Spectrometer from 0.3 to 0.85 AU. J. Geophys. Res. Space Phys. 120, 841–854. doi:10.1002/2014JA020263.
Russell, C.T., et al., 2012. Dawn at Vesta: Testing the protoplanetary paradigm. Science 336, 684–686. doi:10.1126/science.1219381.
Solomon, S.C., et al., 2008. Return to Mercury: A global perspective on MESSENGER's first Mercury flyby. Science 321, 59–62. doi:10.1126/science.1159706.
Starr, R.D., et al., 2012. MESSENGER detection of electron-induced X-ray fluorescence from Mercury's surface. J. Geophys. Res. 117, E00L02. doi:10.1029/2012JE004118.
Stockstill-Cahill, K.R., et al., 2012. Magnesium-rich crustal compositions on Mercury: Implications for magmatism from petrologic modeling. J. Geophys. Res. 117, E00L15. doi:10.1029/2012JE004140.
Vander Kaaden, K.E., McCubbin, F.M., 2015. Exotic crust formation on Mercury: Consequences of a shallow, FeO-poor mantle. J. Geophys. Res. Planets 120, 195–209. doi:10.1002/2014je004733.
Weider, S.Z., et al., 2012. Chemical heterogeneity on Mercury's surface revealed by the MESSENGER X-Ray Spectrometer. J. Geophys. Res. 117. doi:10.1029/2012JE004153.
Weider, S.Z., et al., 2014. Variations in the abundance of iron on Mercury's surface from MESSENGER X-Ray Spectrometer observations. Icarus 235, 170–186. doi:10.1016/j.icarus.2014.03.002.
Weider, S.Z., et al., 2015. Evidence for geochemical terranes on Mercury: Global mapping of major elements with MESSENGER's X-Ray Spectrometer. Earth Planet. Sci. Lett. 416, 109–120. doi:10.1016/j.epsl.2015.01.023.
Yamashita, N., et al., 2013. Distribution of iron on Vesta. Meteorit. Planet. Sci. 48, 2237–2251. doi:10.1111/maps.12139.

Please cite this article as: D.J. Lawrence et al., Compositional terranes on Mercury: Information from fast neutrons, Icarus (2016), http://dx.doi.org/10.1016/j.icarus.2016.07.018